

Binary collision of CMAS droplets—Part II: Unequal-sized droplets

Himakar Ganti¹, Prashant Khare^{1,a)}, Luis Bravo²

¹Department of Aerospace Engineering, University of Cincinnati, Cincinnati, OH 45221-0070, USA

²Vehicle Technology Directorate, Army Research Laboratory, Aberdeen Proving Ground, MD 21005, USA

^{a)}Address all correspondence to this author. e-mail: prashant.khare@uc.edu

Received: 17 April 2020; accepted: 2 June 2020

The analysis presented in Part I of this study on the binary collision of equal molten calcium–magnesium–alumino–silicate (CMAS) droplets is extended to investigate the flow and interfacial dynamics of unequal CMAS droplet collision. Numerical investigations of head-on, off-center, and grazing collisions of two CMAS droplets of size 1 and 2 mm are conducted at pressure and temperature of 20 atm and 1548 K, respectively, that are representative of a gas-turbine combustor. At these conditions, the physical properties of CMAS are density, $\rho_{\text{CMAS}} = 2690 \text{ kg/m}^3$, surface tension between CMAS/air, $\sigma_{\text{CMAS}} = 0.40 \text{ N/m}$, and viscosity, $\mu_{\text{CMAS}} = 11.0 \text{ N-s/m}^2$. The primary difference between the CMAS and a fictitious fluid with viscosity 1/10 of CMAS was higher deformation for the lower viscosity case, leading to stretching and subsequent breakup of the liquid structure. These mechanisms are supported by the time evolution of surface, kinetic, and viscous dissipation energies.

INTRODUCTION

The present work extends the analysis presented in Part I of this study [1], hereafter referred to as Part I, and investigates the interfacial and flow dynamics of binary droplet collision of unequal molten sand particles. Sand and dust particles are routinely ingested in rotorcraft gas-turbine engines, especially during take-off and landing when operating in desert environments. While provisions such as particle separators are installed at the inlets, small particles ($< 50 \mu\text{m}$) are often entrained and reach the combustor. Due to the high operating temperature in the combustion chamber, these particles, in the form of calcium–magnesium–alumino–silicate (CMAS), melt [2, 3, 4]. The undesired entrainment and melting of CMAS particulates is detrimental to the entire engine starting from the compressor to the turbine and causes the loss of efficiency and surge margin in the compressor, clogging of the fuel spray nozzles in the combustor, and clogging of the nozzle vanes and cooling channels in the turbine hot section [3, 5, 6]. The next-generation hot-section material technology based on silicon carbide (SiC) fiber-reinforced SiC/SiC ceramic matrix composites (CMCs), while thermally superior to nickel-based superalloys [7], is susceptible to corrosion from combustion gases and impact from molten CMAS particles, is often coated with environmental [8, 9] and thermal barrier coatings (E/TBC) [3, 10].

Current coatings are effective to 2400 F; however, as combustor temperatures increase to improve efficiencies, next-generation E/TBCs need to be developed that are effective at 3000 F and higher temperatures. Specifically, it is critical to understand the size distribution of CMAS particles leaving the combustion chamber and impacting the hot-section material components to design the coating materials. Molten CMAS droplets in the combustion chamber can undergo stretching, breakup, coalescence, and agglomeration, and these dynamic behaviors determine the shape and size distribution of particles that impact the downstream components in the flow path. Therefore, a detailed understanding of these behaviors and the resulting distributions is imperative, as we develop coatings for future rotorcraft engines.

Much progress has been made on understanding the deposition characteristics and particle trajectories in gas-turbine hot sections [5, 11, 12, 13, 14, 15]; however, limited literature is available for the phenomenon of droplet–droplet interactions of CMAS, while they are still in the combustor. Knowledge of droplet interaction and phenomenon is necessary for developing models for deposition and accretion on surfaces along the hot gas path. In Part I, we discussed the details of the binary collision of equal-sized CMAS droplets. In this manuscript, we investigate CMAS droplet dynamics when two unequal droplets interact.

Most of the previous research efforts on the binary collision of unequal-sized droplets used water and hydrocarbon-based liquid fuels to investigate these phenomena [16, 17, 18, 19, 20]. Tang et al. [18] conducted experiments on unequal tetradecane droplets and showed that for most cases, the smaller droplet gets absorbed into the larger one with interesting flow patterns post-collision. The study also reported that droplet separation occurs when the Weber number is high, and under certain conditions, the smaller droplet exhibits behavior like a jet after being absorbed by the larger droplet. These results are supported by the numerical simulations of Liu et al. [16], Nikolopoulos and Bergeles [21], and Yoshino et al. [22]. As specified in the previous study, the viscosity and surface tension of CMAS are at least two orders of magnitude higher than that of the liquids investigated in the literature; their dynamic behaviors are expected to be significantly different as compared with low viscosity fluids. This hypothesis is based on our previous experience on the dynamics and atomization physics of highly viscous and non-Newtonian fluids [23, 24, 25, 26]. Furthermore, to the best of our knowledge, there are no studies detailing the mechanistic behaviors of off-center and grazing type collisions for unequal droplets, which alongside head-on collisions are equally possible in the hot gas path of a gas-turbine engine.

Therefore, in the current work, we present our investigation on unequal-sized collisions of CMAS droplets. We also compare the effect of viscosity on collisions by conducting numerical computations on a fluid with the same physical properties as CMAS except for viscosity, which is reduced by one-tenth. This is the first study of this kind, the outcomes of which elucidate the collision physics of highly dense and viscous CMAS droplets, and provides estimates for the size and shape distributions of droplets that will interact with turbomachinery blades downstream of the combustor.

The manuscript is organized into 3 sections, namely results and discussions, methodology and conclusions. In the results section, physics associated with the collision of unequal sized CMAS droplets collision in head-on, off-center, and grazing configurations is discussed. The quantitative analysis is based on the temporal evolution of surface, kinetic, and dissipation energies. This is followed by the summary and conclusions drawn from the research effort. In the Methodology section, the governing equations and the computational approach are described in brief; the reader is referred to Part I of this study on equal droplets for a detailed treatment [1]. Model validation and grid sensitivity analyses are detailed in Appendix A.

RESULTS AND DISCUSSIONS

The results are organized into two subsections. First, we will briefly describe relevant non-dimensional numbers and the formulation of various energies that will be used in our analysis.

This will be followed by a discussion of CMAS collision physics both qualitatively using time evolution of the liquid volume fraction defined by $c = 0.5$, and quantitatively using the energy budget and the evolution of kinetic, surface, and viscous dissipation energies. We will also compare and contrast collision behaviors with a fictitious liquid with the same physical properties as CMAS except for the viscosity, which is defined as one-tenth of CMAS.

Relevant nomenclature, non-dimensional numbers, and energies

The phenomenon of droplet collisions is described using Laplace number (La), droplet size ratio (Δ), and an impact parameter (B). The Laplace number estimates the ratio of viscous forces to surface tension forces as follows:

$$La = \left(\frac{We}{Re} \right), \quad (1)$$

where We and Re are the Weber and Reynolds numbers, respectively. The droplet size ratio is defined as follows:

$$\Delta = \left(\frac{d_{small}}{d_{large}} \right). \quad (2)$$

Figure 1 shows the geometric parameters relevant to binary droplet collision. The impact parameter B varies between 0 and 1, where 0 corresponds to head-on and 1 to grazing collision. B can be defined droplets with different diameters D_1 and D_2 , approaching each other with velocity U , and a projected separation χ , given by:

$$B = \left(\frac{\chi}{R_1 + R_2} \right), (R_1 \neq R_2) \quad (3)$$

$$B = \left(\frac{\chi}{2R} \right), (R_1 = R_2).$$

The results will be analyzed using the energy budget that consists of kinetic (KE), surface (SE), and dissipation (DE) energies, similar to the analysis conducted by other researchers in the past [1, 19, 27]. KE of the system is calculated using a volume-weighted sum of the liquid phase kinetic energy, while SE is calculated as the product of the surface tension and interfacial area. DE is defined as the time integral of the volume-weighted sum of the viscous dissipation rate (VDR) given by:

$$VDR, \Phi = \mu \left[2 \left(\frac{\partial u}{\partial x} \right)^2 + 2 \left(\frac{\partial v}{\partial y} \right)^2 + 2 \left(\frac{\partial w}{\partial z} \right)^2 + \left(\frac{\partial v}{\partial x} + \frac{\partial u}{\partial y} \right)^2 \right. \\ \left. + \left(\frac{\partial w}{\partial y} + \frac{\partial v}{\partial z} \right)^2 + \left(\frac{\partial u}{\partial z} + \frac{\partial w}{\partial x} \right)^2 \right] + \lambda \left(\frac{\partial u}{\partial x} + \frac{\partial v}{\partial y} + \frac{\partial w}{\partial z} \right)^2. \quad (4)$$

Here, μ is the viscosity of the liquid phase and λ , based on Stokes' hypothesis, is $-2/3\mu$. For very high Laplace numbers,

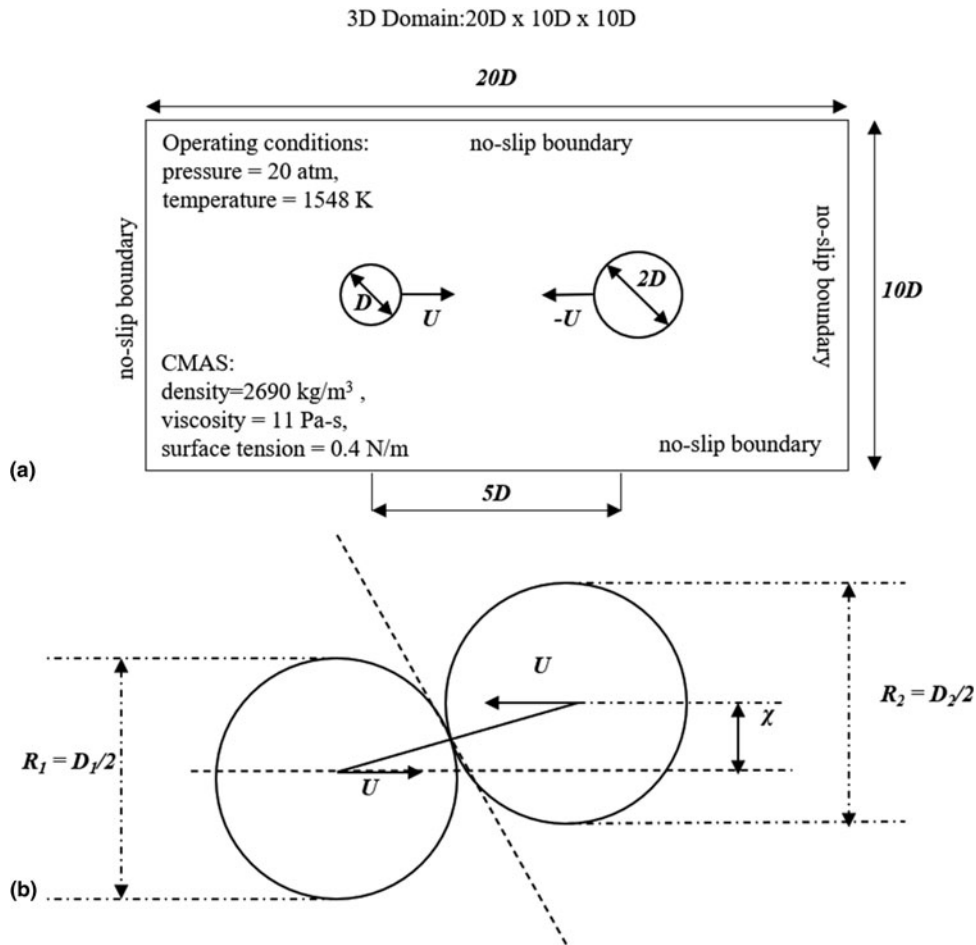


Figure 1: (a) Schematic of the computational setup and (b) relevant geometrical parameters governing droplet collision physics.

such as the current study, VDR is expected to be significantly high [20] which implies that reflexive or stretching separations that are responsible for the breakup of the liquid droplets after coalescence, will be restricted. It should be noted that since the energy equation is not explicitly solved in the current simulations, the sum of KE, SE, and DE will be defined as the total energy, TE. Later in the Results section, the discussion will be based on KE, SE, and DE normalized by the maximum TE during the process.

Physical properties of CMAS and computational setup

The computational domain consists of a $20D \times 10D \times 10D$ box, where D is the diameter of the smaller droplet. All the numerical calculations are conducted at a pressure of 20 atm and a temperature of 1548 K, conditions representative of a gas-turbine combustor. At these conditions, the viscosity and density of air are 5.165×10^{-4} N-s/m² and 4.56 kg/m³, respectively, and the physical properties of CMAS are [6] density, $\rho_{\text{CMAS}} = 2690$ kg/m³, surface tension between CMAS/air, $\sigma_{\text{CMAS}} =$

0.40 N/m, and viscosity, $\mu_{\text{CMAS}} = 11.0$ N-s/m². Two droplets with diameters of 1 and 2 mm are given a velocity of 50 m/s each in the opposite direction for all cases investigated in this paper. To elucidate the effect of viscosity, droplet collision of a fictitious fluid with the same properties as CMAS except for viscosity that is lowered by a factor of 10 is also studied. The Laplace numbers corresponding to CMAS and the fictitious fluid droplet collision are 112.45 and 1.12, respectively.

Physics of binary droplet collision of unequal droplets

In the next three subsections, we will discuss the dynamics of binary unequal droplet collision for CMAS and the fluid that has a viscosity one-tenth that of CMAS in head-on, off-center, and grazing configurations.

Head-on collision ($B = 0.00$)

Figure 1 shows the schematic of the computational setup. CMAS droplets of diameters 1 and 2 mm separated by a distance of 5 mm are given equal and opposite velocities of

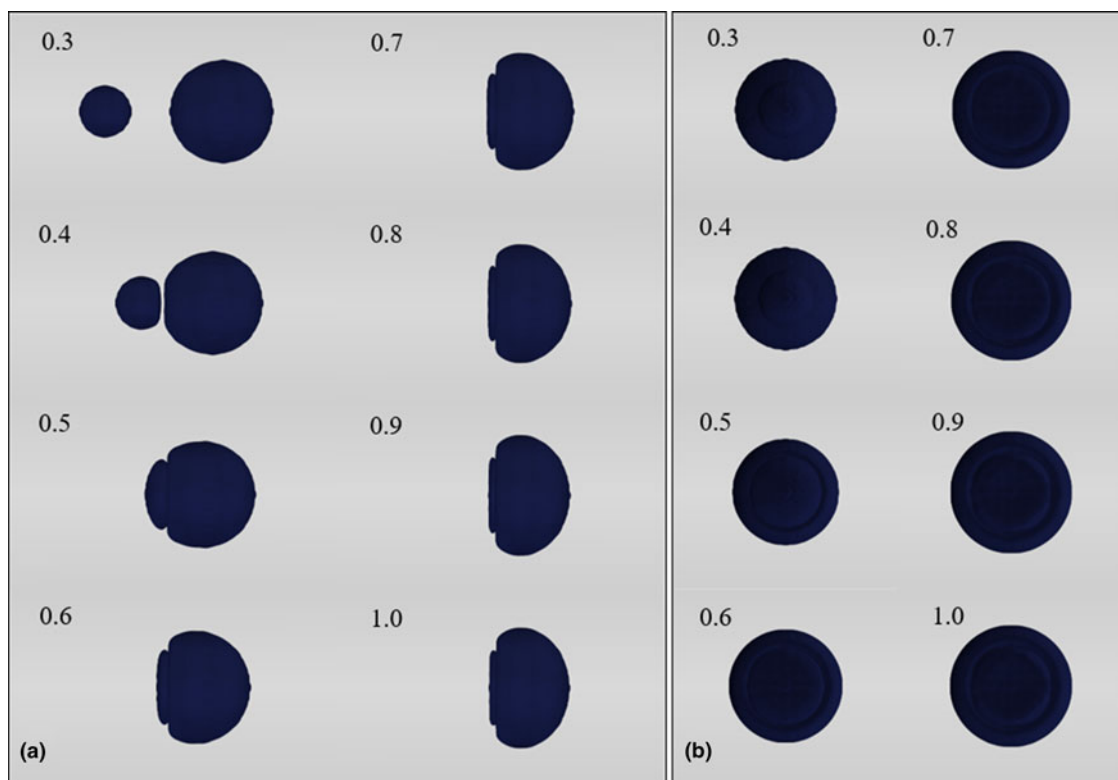


Figure 2: Time evolution of liquid interface when two CMAS droplets collide at an impact factor, $B = 0$. (a) Front view and (b) side view. Non-dimensional time $T = t/(D/U)$.

50 m/s. The corresponding La number is 112.45. Figures 2(a) and 2(b) show, respectively, the front and side views of the time evolution of the liquid interfaces. Initially, during the approach, no apparent deformation is observed because of CMAS's high surface tension and viscosity. This is confirmed quantitatively by the surface energy evolution shown in Fig. 4 (a) that remains horizontal until the droplets come in contact with each other at a non-dimensional time, $T = 0.3$. As the droplets come closer, a gas film is developed between them; however, since the relative velocity is quite high (100 m/s) of this highly dense liquid, the inertial forces overcome this air cushion, expelling it tangentially before the droplets interact. This is followed by deformation and the development of a contact plane. The smaller droplet forms an extrusion disc expanding radially outward from the center while trying to penetrate the larger droplet. The larger droplet deforms into a hemispherical shape. In the final form, the merger of these two droplets looks like a mushroom, with the smaller drop acting like the stock and the larger one as the cap. This mushroom-shaped structure still has significant momentum along the original direction of the larger droplet, and only a part of it is converted to surface and dissipation energies during the collision. This is reflected in the KE plot in Fig. 4(a) that shows a very small drop in the KE after the collision. It has to be noted that even though the droplets merge, the smaller and larger

droplets can still be identified, that is, the larger droplet does not consume the smaller droplet completely. The shape of the combined droplets does not change after the collision, indicating that the droplets have stabilized due to damping from high viscosity and surface tension of CMAS. The overall outcome is partial coalescence along a tangential plane of contact with translation along the original direction of the larger droplet.

In contrast, entirely different sets of events take place when the droplets with one-tenth of the viscosity of CMAS (referred to as $\mu\text{CMAS}/10$) interact, as shown in Fig. 3. As the droplets approach each other, the smaller droplet due to its higher internal pressure penetrates the larger droplet and forms a horizontal bell-shaped structure—the smaller droplet is completely consumed by the larger one. However, due to the extremely high surface tension force, this bell-shaped deformation is retracted and the momentum is transferred in the radial direction that leads to the reduction in the bell protrusion and eventually the formation of a thin circular liquid sheet. This sheet which still has translation motion in the original direction of the larger droplet, radially expands, further reducing the bell size and starts to break up due to capillary effects as ligaments with satellite droplets arranged in concentric circles. This shedding progressively reduces the core and continuously produces ligaments of smaller sizes.

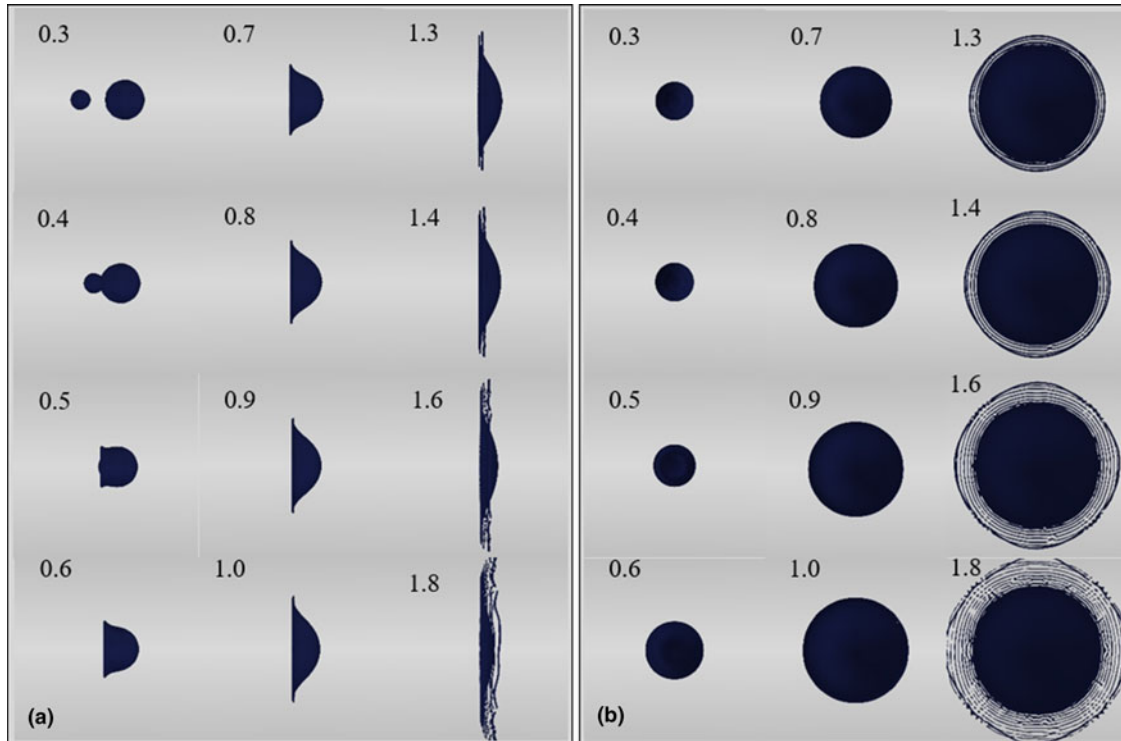


Figure 3: Time evolution of liquid interface when two $\mu\text{CMAS}/10$ droplets collide at an impact factor, $B = 0$. (a) Front view and (b) side view. Non-dimensional time $T = t/(D/U)$.

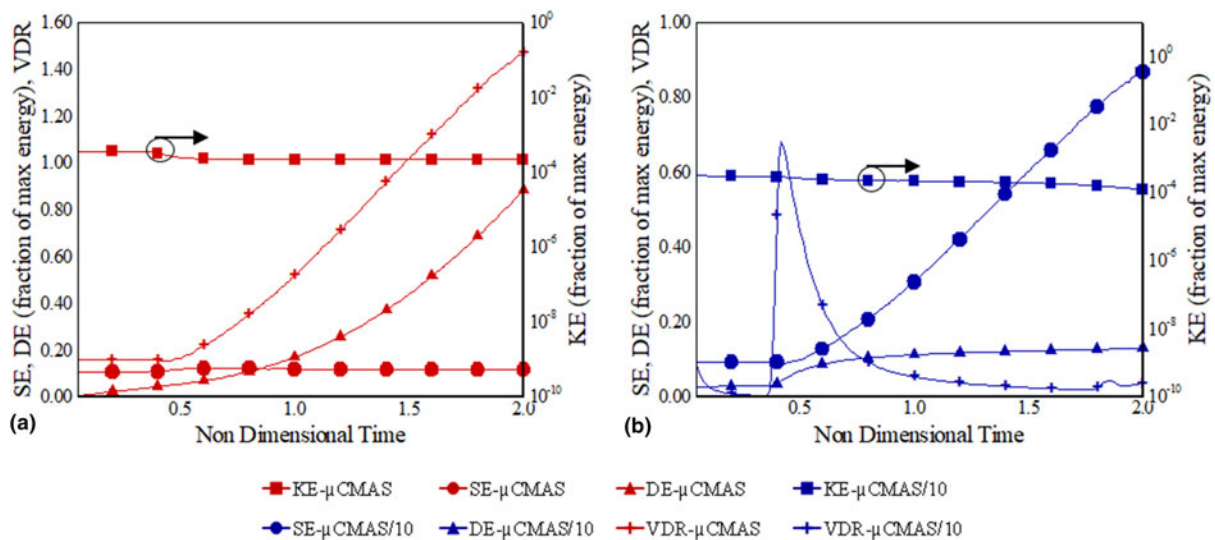


Figure 4: Time evolution of kinetic, surface, dissipation, and viscous dissipation rate for droplet collision at $B = 0.0$ for (a) CMAS droplets and (b) droplets with one-tenth the viscosity of CMAS. Non-dimensional time $T = t/(D/U)$.

In general, as the droplets move and collide, energy transforms between the kinetic, surface, and dissipation. Figure 4(a) shows the energy budget for CMAS droplet collision described in the previous section. As CMAS droplets move toward each other, because of the high surface tension, there is little to no deformation, reflected by no change in surface energy till

$T = 0.3$. During this time, because of the high viscosity, the viscous dissipation rate (VDR) is constant, calculated using Eq. (4); however, DE (time integral of viscous dissipation energy [VDE]) increases steadily. As these viscous droplets come in contact with each other, only a slight decrease in KE is observed. However, DE increases at a much higher rate due

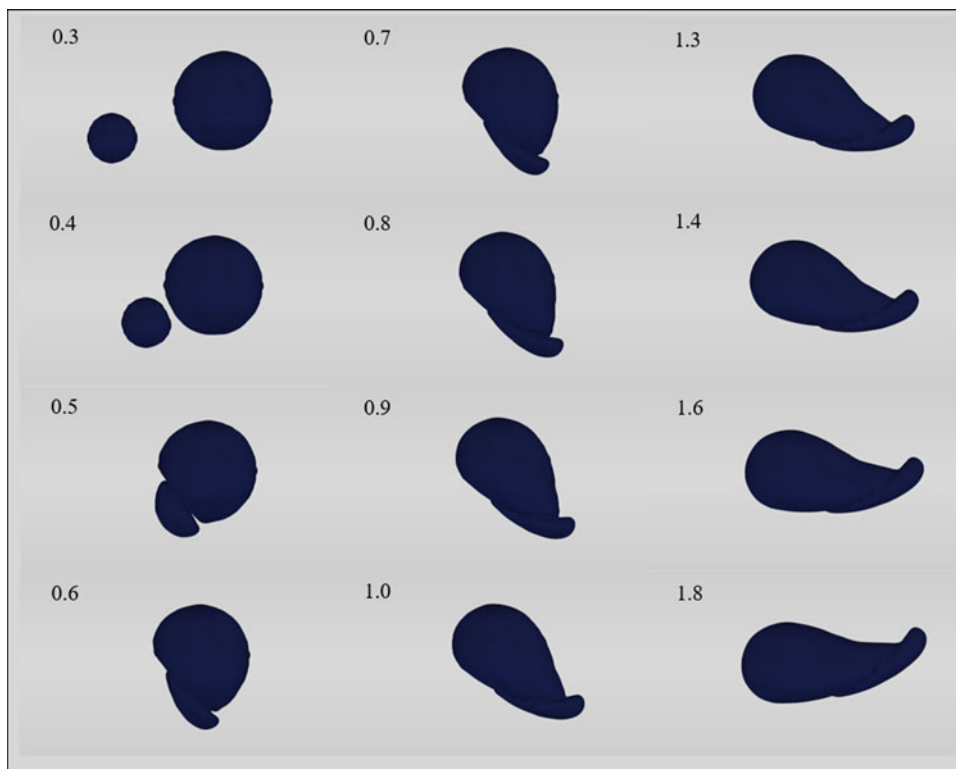


Figure 5: Time evolution of liquid interface when two CMAS droplets collide off-center at an impact factor, $B = 0.5$. Non-dimensional time $T = t/(D/U)$.

to the higher VDR of the droplets. In contrast, for the fictitious liquid ($\mu_{\text{CMAS}/10}$), after the droplets collide, significant deformation takes place because of the lower viscosity, as observed by the evolution of SE in Fig. 4(b). VDR peaks at the time of impact, followed by a rapid decrease. SE increases significantly and supports the deformation and the formation and breakup of multiple circular ligaments.

Off-center collision ($B = 0.50$)

Figure 5 shows the time evolution of the liquid interface for the off-center collision of CMAS droplets corresponding to $B = 0.5$. The operating conditions, including the droplet velocities, are identical to the head-on collision case. The CMAS droplets make tangential contact which is stretched along the lower half of the larger droplet. The contact area increases as the smaller droplet stretch along the surface of the larger droplet. Due to the high surface tension and viscosity of the droplets, they coalesce at the point of contact; however, because of the high inertia, both the droplets still move at their peripheries. As a result, the partially coalesced droplets start to rotate along an axis through the contact point and parallel to the contact plane. Stretching separation is not observed for this configuration owing to high viscosity and surface tension, which also prevents any further breakup of either the larger or smaller droplet. These trends are also observed in the energy budget

shown in Fig. 7(a), which in general is similar to that of the head-on collision, except that the SE, in this case, increases by a tiny bit after the point of contact because of stretching. It should be noted that the energies are normalized, so all the energy budget plots show the relative importance of each of the components. The VDR increasing monotonically, which supports our previously stated conjecture that viscous forces dissipate the impact of the collision significantly to avoid breakup of the droplets.

As shown in Fig. 6, the initial events as droplets of the fictitious liquid ($\mu_{\text{CMAS}/10}$) approach each other at $B = 0.5$ are similar to that of CMAS in that neither droplet deforms before the collision. As the droplets start to interact, a collision plane is formed which is tangential to the initial contact point. Deformation of the smaller droplet leads to the formation of an extrusion disc that expands and stretches along the contact plane and away from the fluid bulk of the larger droplet. Due to the lower viscosity of the fictitious fluid, an elongated rim with a thinning lamellar disc is formed. As the larger droplet continues to move further away due to inertia, it expands both the rim and the lamella. This leads to the rupture of the lamella followed by relaxation of the disc toward the larger droplet due to surface tension and breaks up into smaller droplets. The side view, shown in Fig. 6(b), resembles the beads-on-a-string phenomena. As this ensemble stretches further, there is a continuous production of droplets in the contact plane increasing

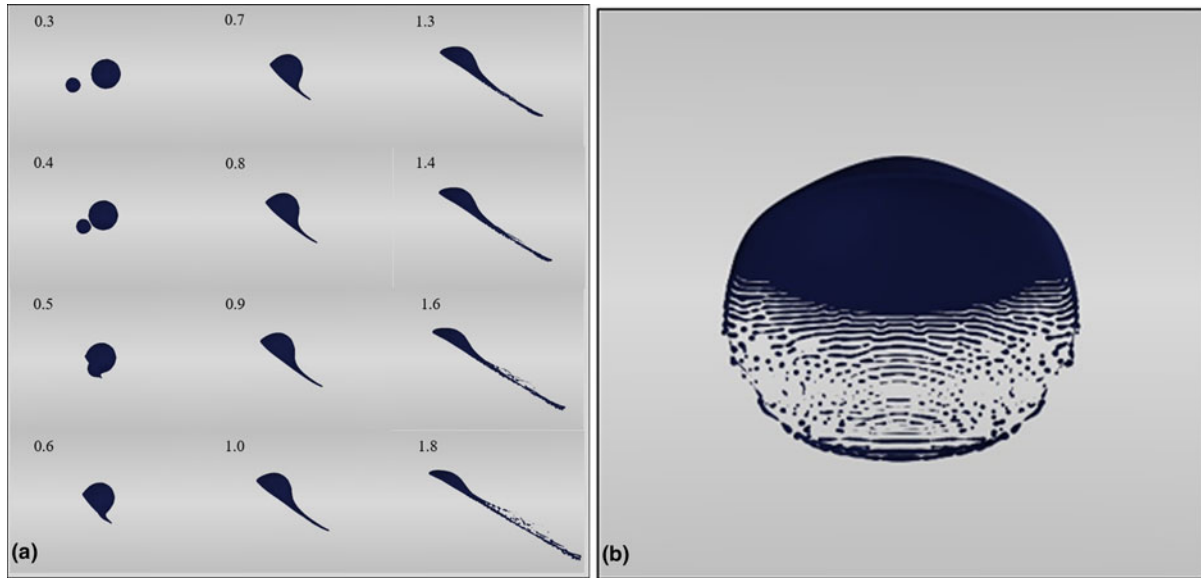


Figure 6: (a) Time evolution of liquid interface when two μ CMAS/10 droplets collide off-center at an impact factor, $B = 0.5$; (b) zoomed side view of liquid interface at $T = 1.6$ showing beads-on-a-string type structures. Non-dimensional time $T = t/(D/U)$.

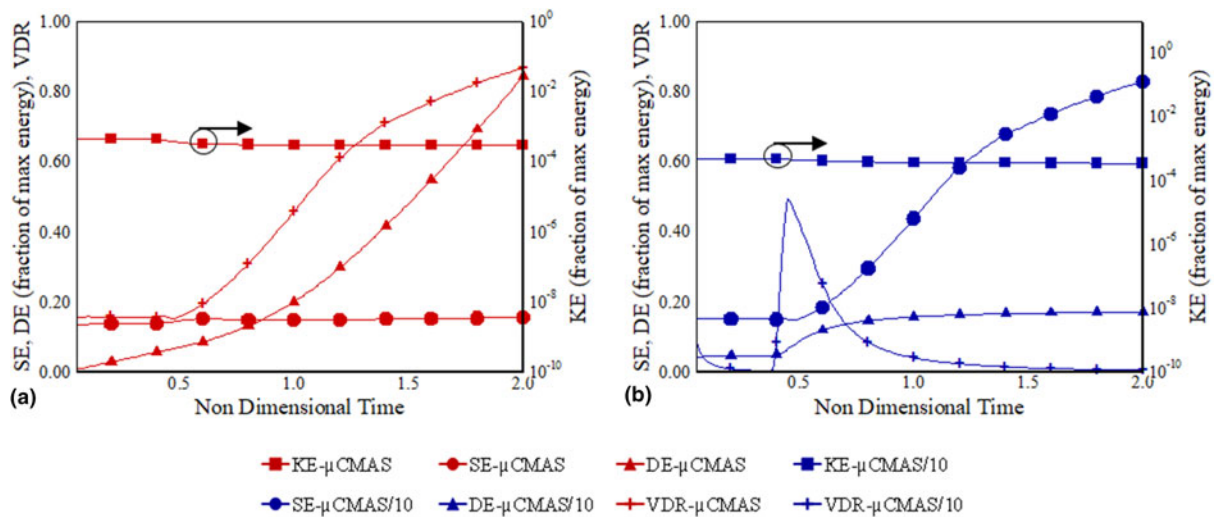


Figure 7: Time evolution of kinetic, surface, dissipation, and viscous dissipation rate for droplet collision at $B = 0.5$ for (a) CMAS droplets and (b) droplets with one-tenth the viscosity of CMAS. Non-dimensional time $T = t/(D/U)$.

the total surface area, and hence the surface energy. As shown in Fig. 7, the VDR peaks at the point of impact, and the DE becomes constant after $T = 1$. This indicates that viscous dissipation is unable to damp the inertial forces sufficiently leading to break up, which results in a large increase in SE after the collision.

Grazing collision ($B = 0.80$)

Figure 8 shows the temporal evolution of the liquid interface when two unequal CMAS droplets undergo a grazing collision, corresponding to $B = 0.8$. Similar to the off-center collision at $B = 0.5$, the droplets approach each other and while sliding

along the tangential contact surface. This creates a tear-drop shape for both the droplets, and they adhere to each other creating a central ligament connecting them. This central ligament starts to stretch, as the high inertia of both droplets is not sufficiently damped during the collision. In addition, similar to the off-center case, a rotational motion is imparted to the combined structure. This ligament keeps on stretching, as the droplets move away. As the ligament thins, pinch-off eventually leads to the formation of multiple satellite droplets. While the large droplet somewhat maintains its spherical shape, at least at the top, the smaller droplet flattens to form a disk. The energy budget for this case, as shown in Fig. 10(a),

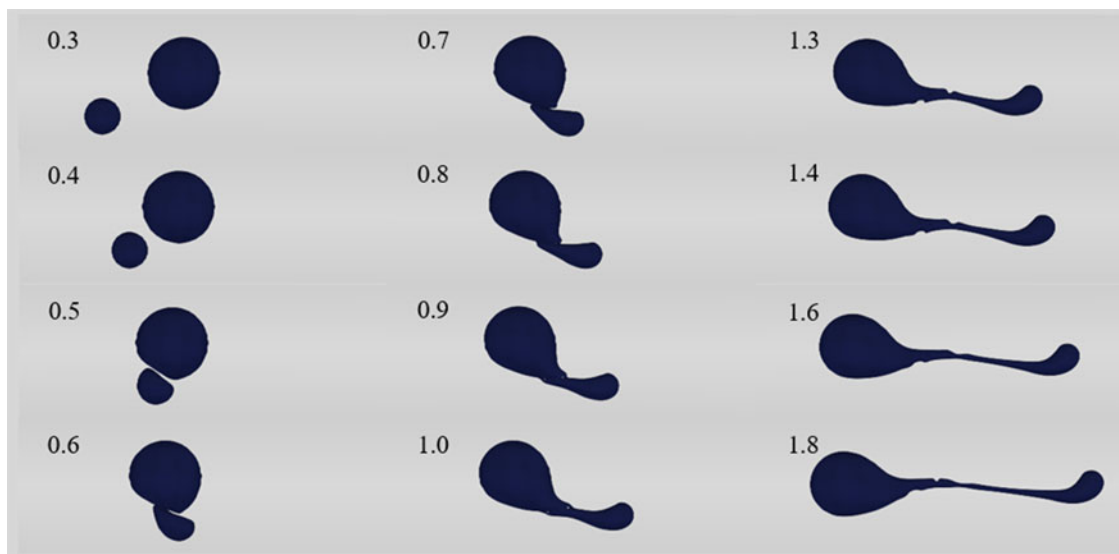


Figure 8: Time evolution of liquid interface for grazing droplet collision at an impact factor, $B = 0.8$ for CMAS droplets. Non-dimensional time $T = t/(D/U)$.

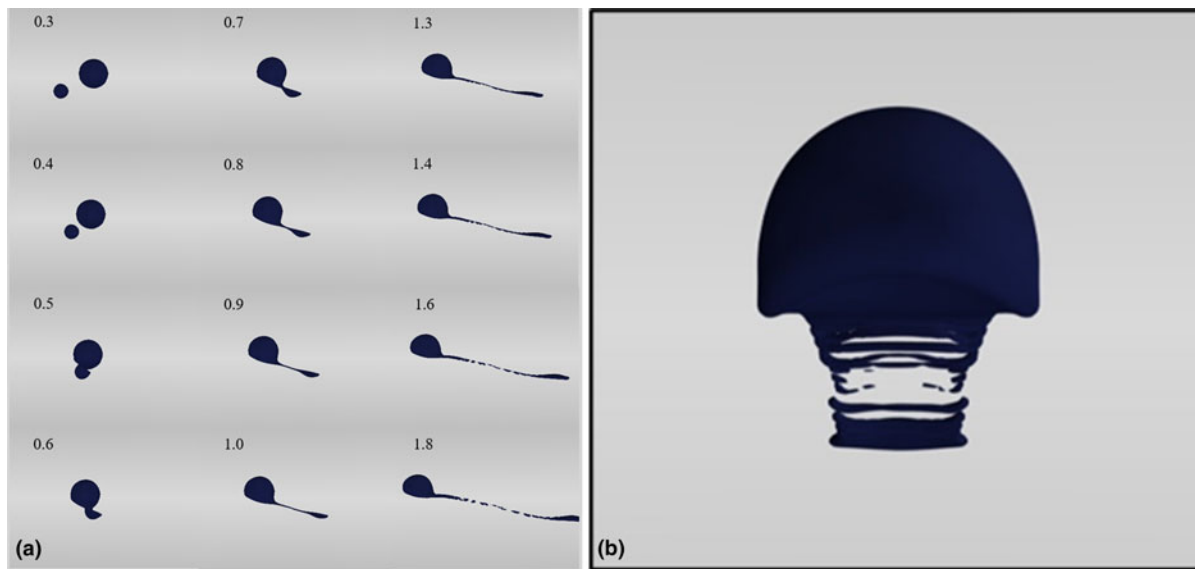


Figure 9: (a) Time evolution of liquid interface when two $\mu\text{CMAS}/10$ droplets collide off-center at an impact factor, $B = 0.8$; (b) zoomed side view of liquid interface at $T = 1.6$ showing beads-on-a-string type structures. Non-dimensional time $T = t/(D/U)$.

supports these observations. A gradual increase in SE is observed with no significant change in KE. A peak in VDR is observed, which then becomes steady after the collision. This indicates that the viscous forces are unable to damp the inertial forces and breakup occurs as the droplets stretch away from each other.

Figure 9 shows the time evolution of the fictitious liquid ($\mu\text{CMAS}/10$) for $B = 0.8$. Compared with CMAS under the same conditions, contact is established earlier during the collision. However, the time evolutions of the rest of the interfacial features are qualitatively similar to that of CMAS droplet collision at $B = 0.8$, except that the central ligament is much thinner

and the subsequent droplets that are formed after the pinch-off are smaller. Both these differences are because of the lower viscosity of the fictitious fluid. This is supported by the VDR peak followed by a rapid fall which indicates that viscous forces are unable to damp the inertial forces significantly to prevent breakup (which was the case for CMAS at $B = 0.8$). These trends are shown in Fig. 10b.

SUMMARY AND FUTURE WORK

Binary collisions of unequal-sized CMAS droplets ($\Delta = 0.5$) for three different impact parameters ($B = 0.0, 0.5, 0.8$) were

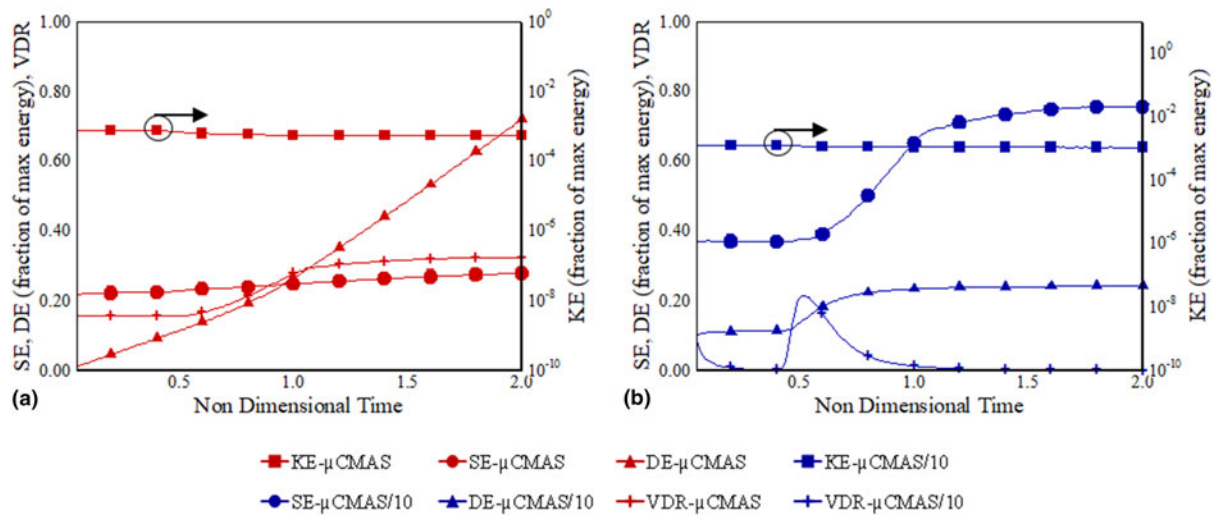


Figure 10: Time evolution of kinetic, surface, dissipation, and viscous dissipation rate for droplet collision at $B=0.8$ for (a) CMAS droplets and (b) droplets with one-tenth the viscosity of CMAS. Non-dimensional time $T = t/(D/U)$.

numerically simulated at conditions representative of a gas-turbine combustor to elucidate the fundamental processes and mechanisms that dictate their interactions. CMAS is in liquid form at these conditions and, therefore, was modeled as a liquid with appropriate density, viscosity, and surface tension—these physical properties have been previously reported in the literature. To identify the effect of the high viscosity of CMAS (it should be noted that the surface tension and viscosity of CMAS are at least two orders of magnitude higher than most hydrocarbons), a fictitious fluid with all properties identical to CMAS except viscosity, which was reduced by a tenth, was also studied. The droplets are given with an initial velocity of 50 m/s, as they approach each other either head-on or off-center. A summary of the three configurations investigated in this manuscript is below:

(i) $B = 0$: CMAS droplets result in partial coalescence, while binary collision of the fictitious liquid (with 1/10th the viscosity) results in the formation of a thin liquid sheet that sheds ligaments and droplets in concentric circles around a core.

(ii) $B = 0.5$: Both CMAS and the fictitious fluid result in the formation of an unsymmetrical dumbbell shape. While for CMAS droplets, this shape remains intact, for the other fluid, due to its lower viscosity, the dumbbell stretches and breaks up forming ligaments and satellite droplets.

(iii) $B = 0.8$: Similar to $B = 0.5$, in this case too, both CMAS and the fictitious fluid behavior are qualitatively the same. The differences are in terms of the central ligament thickness and the size of droplets produced after pinch-off, which are larger in the case of CMAS binary collision.

In a subsequent paper, we will present the droplet size and shape statistics produced after the collision of both equal- and unequal-sized droplets. Further, a general model will be

developed that can be incorporated in large scale simulations that include hundreds of thousands of droplets.

METHODOLOGY

Current research poses two stringent challenges that need to be addressed to quantitatively identify the underlying physical processes present when two CMAS droplets interact. The challenges are (i) the presence of multiple phases and frequent interfacial topology changes and (ii) the existence of widely disparate length and time scales that need to be resolved in an accurate and computationally efficient manner. To accurately address the first issue, the most appropriate approach to investigate the flow physics of interest with high-fidelity is based on the Eulerian–Eulerian framework, that is, all relevant phases (liquid and gaseous) being treated as continuous, and the interface between them is captured. This approach is also called the one-fluid approach in the literature [28]. To appropriately resolve the wide range of spatial and temporal scales, an adaptive mesh refinement methodology is adopted such that high resolution is achieved in reasonable turnaround time. Based on this rationale, the next subsection details the theoretical framework and numerical methods that are used in this research effort.

Governing equations

The formulation is based on the three-dimensional, incompressible, variable-density form of the Navier–Stokes equations with surface tension. The mass conservation equation is given by:

$$\frac{\partial \rho}{\partial t} + \vec{u} \cdot \nabla \rho = 0, \quad (5)$$

which, considering incompressibility, becomes

$$\vec{\nabla} \cdot \vec{u} = 0. \quad (6)$$

Conservation of momentum is given as follows:

$$\frac{\partial \rho \vec{u}}{\partial t} + \nabla \cdot (\rho \vec{u} \vec{u}) = -\nabla p + \nabla \cdot \tilde{\tau} + \vec{F}_{st}, \quad (7)$$

where F_{st} is the surface tension force per unit volume and τ is the shear stress tensor:

$$\tilde{\tau} = \mu(\nabla \vec{u} + (\nabla \vec{u})^T). \quad (8)$$

A state-of-the-art, high-resolution, volume-of-fluid (VOF) interface capturing method is adopted for large-scale interfacial evolution. Surface tension is accommodated as a Dirac distribution function on the interface. Governing equations are written in an Eulerian reference frame to capture the gas–liquid interface. A VOF scalar variable c to trace the multi-fluid interface is given as follows:

$$c = \begin{cases} 0 & \text{fluid 1} \\ 1 & \text{fluid 2} \end{cases} \quad (9)$$

Density and viscosity for each computational cell are defined as linear functions of c as follows:

$$\begin{aligned} \rho(c) &= c\rho_1 + (1 - c)\rho_2 \\ \mu(c) &= c\mu_1 + (1 - c)\mu_2 \end{aligned} \quad (10)$$

The advection equation for density can then be written as an equivalent equation for the volume fraction:

$$\frac{\partial c}{\partial t} + (\vec{u} \cdot \nabla c) = 0. \quad (11)$$

The conservation equations are written for the different phases without using the jump condition at the interface, which translates to singularities in the governing equations. It can be shown that this formulation is equivalent to that written for each phase separately with the pressure jump condition at the interface. As pointed out by Tryggvason et al. [28], the one-fluid approach can be interpreted in two ways, in a weak sense, in which the governing equations are satisfied only in the integral form, or by admitting solutions using step and delta functions. In this study, we use the latter approach by modeling the surface tension effects using the continuum surface force model developed by Brackbill et al. [29],

$$\vec{F}_{st}(\vec{x}_1) = \sigma \int_S \kappa(\vec{x}_2) \hat{n}(\vec{x}_2) \delta(\vec{x}_1 - \vec{x}_2) dS. \quad (12)$$

where σ is the surface tension force, κ is the local curvature,

and δ is the Dirac delta function. κ is evaluated as follows:

$$\kappa = \frac{1}{R_1} + \frac{1}{R_2}. \quad (13)$$

where R_1, R_2 are principal radii of curvature. Surface tension force for each cell at the interface is approximated by:

$$\vec{F}_{st} \approx \sigma \kappa \delta \hat{n}. \quad (14)$$

The reader is referred to the first part of this study for a detailed treatment of governing equations, numerical methods, and mesh adaptation.

Acknowledgments

The authors gratefully acknowledge the Advanced Computing Center at the University of Cincinnati, and the DoD High Performance Computing Modernization Program (HPCMP) subproject number, ARLAP44862H70 for the computational resources. Luis Bravo was supported by the US Army Research Laboratory 6.1 basic research program in propulsion sciences.

References

- H. Ganti, P. Khare, and L. Bravo:** Binary collision of CMAS droplets—Part I: Equal sized droplets. *J. Mater. Res. (Focus Issue - Sandphobic Thermal/Environmental Barrier Coatings for Gas Turbine Engines)*, 1–15 (2020). doi:10.1557/jmr.2020.138.
- A. Ghoshal, M. Murugan, M.J. Walock, A. Nieto, B.D. Barnett, M.S. Pepi, J.J. Swab, D. Zhu, K.A. Kerner, C.R. Rowe, C.Y. Shiao, D.A. Hopkins, and G. A. Gazonas:** Molten particulate impact on tailored thermal barrier coatings for gas turbine engine. *J. Eng. Gas Turb. Power* **140** (2018).
- M. Murugan, A. Ghoshal, A. Nieto, M. Walock, L. Bravo, N. Jain, M. Pepi, J. Swab, D. Zhu, R.T. Pegg, C. Rowe, A. Flatau, and K. Kerner:** Prevention of molten sand attack on thermal barrier coatings for rotorcraft gas turbine blades—A round robin test evaluation. In *Annual Forum Proceedings* (AHS International, Fairfax, VA, USA, 2018).
- N. Libertowski, N. Plewacki, and J.P. Bons:** The effect of temperature and melting relative to particle deposition in gas turbines. In *AIAA Scitech 2019 Forum*, Jan 7 to 11, San Diego, CA, USA (American Institute of Aeronautics and Astronautics, Reston, VA, USA, 2019).
- L.G. Bravo, Q. Xue, M. Murugan, A. Ghoshal, M. Walock, and A. Flatau:** Particle transport analysis of sand ingestion in gas turbine jet engines. In *53rd AIAA/SAE/ASEE Joint Propulsion Conference*, Jul 10 to Jul 12, Atlanta, GA, USA (AIAA, Reston, VA, USA, 2017); pp. 1–14.

6. **N. Jain, L. Bravo, S. Bose, D. Kim, M. Murugan, A. Ghoshal, and A. Flatau:** Turbulent multiphase flow and particle deposition of sand ingestion for high-temperature turbine blades. In *Proceedings of the Summer Program*, Jun 24 to Jul 20, Stanford, CA, USA (Center for Turbulence Research, Stanford, CA, USA, 2018); pp. 35–44.
7. **I. Spitsberg, and J. Steibel:** Thermal and environmental barrier coatings for SiC/SiC CMCs in aircraft engine applications*. *Int. J. Appl. Ceram. Technol.* **1**(4), 291–301 (2004).
8. **K.N. Lee, D.S. Fox, J.I. Eldridge, D. Zhu, R.C. Robinson, N.P. Bansal, and R.A. Miller:** Upper temperature limit of environmental barrier coatings based on mullite and BSAS. *J. Am. Ceram. Soc.* **86**(8), 1299–1306 (2003).
9. **K.N. Lee:** Current status of environmental barrier coatings for Si-based ceramics. *Surf. Coat. Technol.* **133–134**, 1–7 (2000).
10. **M. Murugan, A. Ghoshal, M. Walock, A. Nieto, L. Bravo, B. Barnett, M. Pepi, J. Swab, R.T. Pegg, C. Rowe, D. Zhu, and K. Kerner:** Microstructure based material-sand particulate interactions and assessment of coatings for high temperature turbine blades. In *Proceedings of ASME Turbo Expo (IGTI)*, Charlotte, NC USA (ASME, New York, NY, USA, 2017).
11. **D.K. Larry Fehrenbacher, J. Kutsch, I. Vesnovsky, E. Fehrenbacher, A. Ghoshal, M. Walock, M. Murugan, and A. Nieto:** Advanced environmental barrier coatings for SiC CMCs. In *Advances in Ceramics for Environmental, Functional, Structural, and Energy Applications II*, Vol. **266**, edited by M.M. Mahmoud, K. Sridharan, H. Colorado, A.S. Bhalla, J.P. Singh, S. Gupta, J. Langhorn, A. Jitianu, and N. Jose Manjoooran (John Wiley & Sons, Hoboken, NJ, USA, 2019); pp 83–93.
12. **W. Song, S. Yang, M. Fukumoto, Y. Lavallée, S. Lokachari, H. Guo, Y. You, and D.B. Dingwell:** Impact interaction of in-flight high-energy molten volcanic ash droplets with jet engines. *Acta Mater.* **171**, 119–131 (2019).
13. **S. Singh and D. Tafti:** Particle deposition model for particulate flows at high temperatures in gas turbine components. *Int. J. Heat Fluid Flow* **52**, 72–83 (2015).
14. **D. Pearson and R. Brooker:** The accumulation of molten volcanic ash in jet engines, simulating the role of magma composition, ash particle size and thermal barrier coatings. *J. Volcanol. Geotherm. Res.* **389**, 106707 (2020).
15. **L. Bravo, N. Jain, P. Khare, M. Murugan, A. Ghoshal, and A. Flatau:** Physical aspects of particle dynamics and deposition in turboshaft engines. *J. Mater. Res.* (under review), (2020).
16. **D. Liu, P. Zhang, C.K. Law, and Y. Guo:** Collision dynamics and mixing of unequal-size droplets. *Int. J. Heat Mass Transfer* **57**, 421–428 (2013).
17. **C. Tang, J. Zhao, P. Zhang, C.K. Law, and Z. Huang:** Dynamics of internal jets in the merging of two droplets of unequal sizes. *J. Fluid Mech.* **795**, 671–689 (2016).
18. **C. Tang, P. Zhang, and C.K. Law:** Bouncing, coalescence, and separation in head-on collision of unequal-size droplets. *Phys. Fluids* **24**, 22101-1–22101-15 (2012).
19. **K.-L. Pan, C.K. Law, and B. Zhou:** Experimental and mechanistic description of merging and bouncing in head-on binary droplet collision. *J. Appl. Phys.* **103**, 064901 (2008).
20. **N. Ashgriz and J.Y. Poo:** Coalescence and separation in binary collisions of liquid drops. *J. Fluid Mech.* **221**, 183–204 (1990).
21. **N. Nikolopoulos and G. Bergeles:** The effect of gas and liquid properties and droplet size ratio on the central collision between two unequal-size droplets in the reflexive regime. *Int. J. Heat Mass Transfer* **54**, 678–691 (2011).
22. **M. Yoshino, J. Sawada, and K. Suzuki:** Numerical simulation of head-on collision dynamics of binary droplets with various diameter ratios by the two-phase lattice kinetic scheme. *Comput. Fluids* **168**, 304–317 (2018).
23. **V. Notaro, P. Khare, and J.G. Lee:** Mixing characteristics of non-Newtonian impinging jets at elevated pressures. *Flow Turbul. Combust.* **102**, 355–372 (2019).
24. **P. Khare and V. Yang:** Newtonian and non-newtonian liquid droplet breakup: Child droplet statistics. *Proceedings of ICLASS 2015, 13th Triennial International Conference on Liquid Atomization and Spray Systems*, Aug 23 to Aug 27, Tainan, Taiwan (2015).
25. **P. Khare and V. Yang:** Breakup of non-newtonian liquid droplets. In *44th AIAA Fluid Dynamics Conference*, Jan 16 to Jan 20, Atlanta, GA, USA (AIAA, Reston, VA, USA, 2014).
26. **J. Gamertsfelder, P. Khare, and L.G. Bravo:** Investigation of atomization behaviour of liquid monopropellants in pintle injectors. In *ASME Turbo Expo*, June 22–26, London, England (ASME, New York, NY, USA, 2020).
27. **X. Chen, D. Ma, P. Khare, and V. Yang:** Energy and mass transfer during binary droplet collision. In *49th AIAA Aerospace Sciences Meeting including the New Horizons Forum and Aerospace Exposition*, Jan 4 to Jan 7, Orlando, FL, USA (AIAA, Reston, VA, USA, 2011); pp. 1–14.
28. **G. Tryggvason, R. Scardovelli, and S. Zaleski:** *Direct Numerical Simulations of Gas–Liquid Multiphase Flows* (Cambridge University Press, New York, NY, USA, 2011).
29. **J.U. Brackbill, D.B. Kothe, and C. Zemach:** A continuum method for modeling surface tension. *J. Comput. Phys.* **100**, 335–354 (1992).

APPENDIX A: COMPUTATIONAL CHALLENGES, MODEL VALIDATION, AND GRID-SENSITIVITY ANALYSIS

Irrespective of the numerical method, the challenges accompanying the numerical simulation of incompressible two-phase systems increase dramatically, as the density ratio increases [1, 2]. The time integration scheme used in the current approach involves a classical time-splitting projection method, which requires the solution of the Poisson equation to obtain the pressure field:

$$\nabla \cdot \left[\frac{\Delta t}{\rho_{n+\frac{1}{2}}} \nabla p_{n+\frac{1}{2}} \right] = \nabla \cdot u_* \quad (A1)$$

Equation (A1) is solved using a standard multigrid V-cycle methodology, and for large density and viscosity ratios, its solution suffers from slow convergence rates. One of the ways to overcome this issue is by using high grid resolution to resolve the steep density and viscosity gradients at the interface to ensure consistency in the momentum equation. Another method of speeding up the convergence rate is to spatially filter the interface during reconstruction. Even though the current methodology performs very well for the current configuration of droplet interaction at high viscosity and density ratios, the convergence can seriously degrade, depending on the problem and interface topology [3], in comparison with other methods [4]. Therefore, for all the

cases conducted as a part of this research effort, including the validation study described in the next section, we have used both the aforementioned strategies to ensure accuracy: high grid resolution and spatially filtering (at least once) to ensure numerical accuracy and adequate resolution of the gas–liquid interface.

As a first step, grid-sensitivity analysis which is conducted to ensure appropriate grid resolution is used to resolve the physics under consideration. The canonical configuration of equal CMAS droplets colliding head-on ($B = 0.0$) is selected for the grid-sensitivity study. Figure A1 shows a comparison of the liquid morphology for four different refinement levels described below:

- (i) level 6 at liquid/gas interface, level 5 for the droplet interior, and level 3 for the rest of the domain—L6
- (ii) level 7 at liquid/gas interface, level 6 for the droplet interior, and level 3 for the rest of the domain—L7
- (iii) level 8 at liquid/gas interface, level 7 for the droplet interior, and level 4 for the rest of the domain—L8
- (iv) level 9 at liquid/gas interface, level 8 for the droplet interior, and level 5 for the rest of the domain—L9

As seen clearly, L6 is unable to refine the interface sufficiently. While L7 resolves the interface better, to ensure that the gas film when the droplets come closer to each other is resolved, L8 and L9 were investigated, which show almost identical results for interface deformation and evolution as well as the gas film. Therefore, for this study, L8 was selected as the grid resolution. While for high Weber number droplet collision, such as the current study, bouncing is not

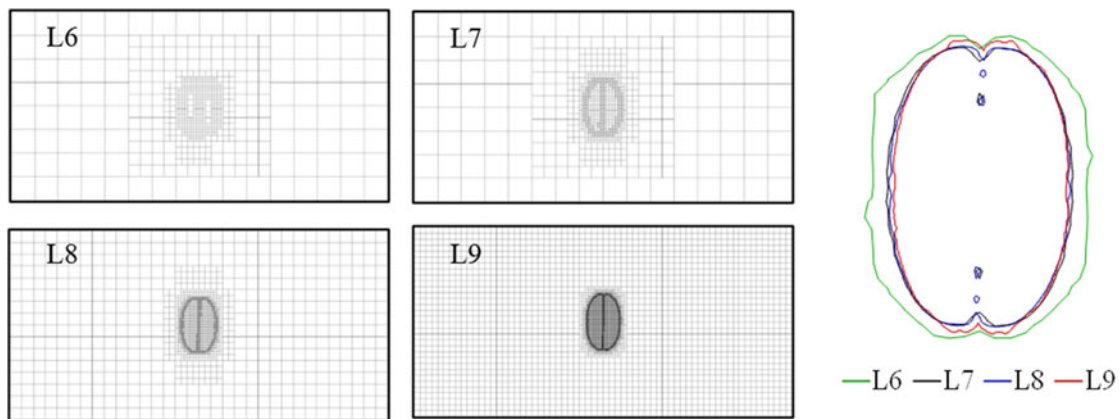


Figure A1: Grid-sensitivity study based on levels 6, 7, 8, and 9. The figure on the right shows an overlay of the liquid interface for these levels.

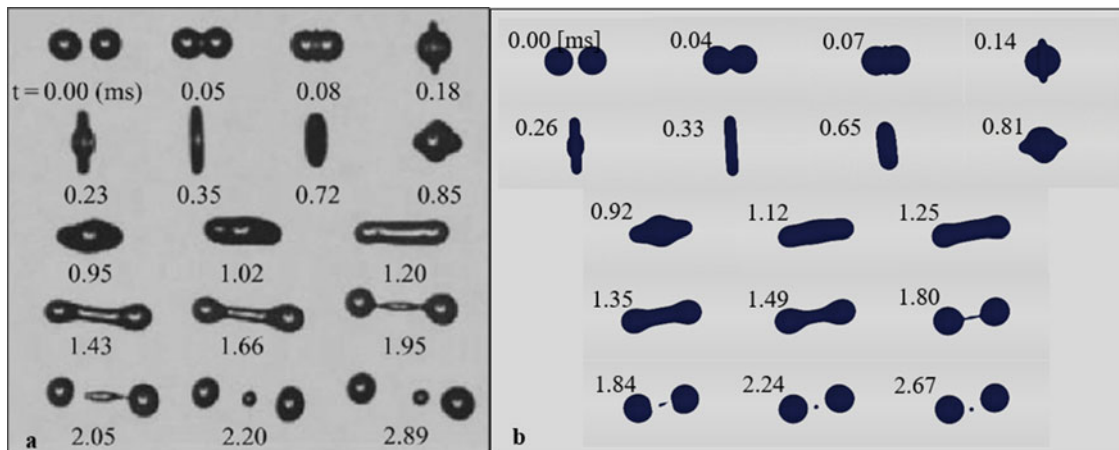


Figure A2: Time evolution of liquid interface when two tetradecane droplets collide at an impact factor, $B = 0.06$. (a) Experimental images of Qian and Law [5] shown on the left and (b) results from current simulations.

expected to be an outcome, in addition to gradient and value-based refinements, distance-based refinement is employed to ensure that the gas film is resolved accurately.

Next, model validation is conducted by simulating the experiments conducted by Qian and Law [5]. It should be noted that since no study in the past has investigated CMAS droplet collision, we have to resort to using data on tetradecane droplet collision for validation purposes. We chose a case that incorporates merging, retracting, and formation of satellite droplets to ensure that our framework can accurately model different aspects of the droplet collision phenomena. In this experiment, conducted at a pressure of 1 atm and 300 K, two droplets of diameter 336 μm with 2.48 m/s collide. The density and viscosity of air at these conditions are 1.18 kg/m^3 and $1.79 \times 10^{-4} \text{ N}\cdot\text{s}/\text{m}^2$, respectively. The density, viscosity, and surface tension of tetradecane are 785.88 kg/m^3 , $2.21 \times 10^{-3} \text{ N}\cdot\text{s}/\text{m}^2$, and 0.02656 N/m. Figure A2 shows the time evolution of events that take place, as these droplets collide. The left side shows the experimental measurements and the right side shows results from the current simulation, showing excellent comparison. All flow features, including droplet coalescence, ligament formation and elongation, subsequent separation by pinching, and satellite droplet formation, are accurately captured.

Details of grid-sensitivity and experimental validation can be found in the previous article for Binary Collision of CMAS Droplet – Part I: Equal Sized Droplets [6].

References

1. **O. Desjardins and V. Moureau:** Methods for multiphase flows with high density ratio. In *Proceedings of the Summer Program*, Jun 27 to Jul 23, Stanford, CA, USA (Center for Turbulence Research, Stanford, CA, USA, 2010); pp. 313–322.
2. **M. Gorokhovski and M. Herrmann:** Modeling primary atomization. *Annu. Rev. Fluid Mech.* **40**, 343–366 (2008).
3. **S. Popinet:** An accurate adaptive solver for surface-tension-driven interfacial flows. *J. Comput. Phys.* **228**, 5838–5866 (2009).
4. **D. Gerlach, G. Tomar, G. Biswas, and F. Durst:** Comparison of volume-of-fluid methods for surface tension-dominant two-phase flows. *Int. J. Heat Mass Transfer* **49**, 740–754 (2006).
5. **J. Qian and C.K. Law:** Regimes of coalescence and separation in droplet collision. *J. Fluid Mech.* **331**, 59–80 (1997).
6. **H. Ganti, P. Khare, and L. Bravo:** Binary collision of CMAS droplets-Part I: Equal sized droplets. *J. Mater. Res.* (Focus Issue – Sandphobic Thermal/Environmental Barrier Coatings for Gas Turbine Engines), 1–15 (2020). doi:10.1557/jmr.2020.138